

## How drugs modulate the performance of the human heart

Peirlinck, Mathias; Yao, J.; Sahli Costabal, F.; Kuhl, E.

**DOI**

[10.1007/s00466-022-02146-1](https://doi.org/10.1007/s00466-022-02146-1)

**Publication date**

2022

**Document Version**

Final published version

**Published in**

Computational Mechanics

**Citation (APA)**

Peirlinck, M., Yao, J., Sahli Costabal, F., & Kuhl, E. (2022). How drugs modulate the performance of the human heart. *Computational Mechanics*, 69(6), 1397-1411. <https://doi.org/10.1007/s00466-022-02146-1>

**Important note**

To cite this publication, please use the final published version (if applicable).  
Please check the document version above.

**Copyright**

Other than for strictly personal use, it is not permitted to download, forward or distribute the text or part of it, without the consent of the author(s) and/or copyright holder(s), unless the work is under an open content license such as Creative Commons.

**Takedown policy**

Please contact us and provide details if you believe this document breaches copyrights.  
We will remove access to the work immediately and investigate your claim.

***Green Open Access added to TU Delft Institutional Repository***

***'You share, we take care!' - Taverne project***

**<https://www.openaccess.nl/en/you-share-we-take-care>**

Otherwise as indicated in the copyright section: the publisher is the copyright holder of this work and the author uses the Dutch legislation to make this work public.



# How drugs modulate the performance of the human heart

M. Peirlinck<sup>1,2</sup> · J. Yao<sup>3</sup> · F. Sahli Costabal<sup>4</sup> · E. Kuhl<sup>5</sup>

Received: 12 August 2021 / Accepted: 19 January 2022

© The Author(s), under exclusive licence to Springer-Verlag GmbH Germany, part of Springer Nature 2022

## Abstract

Many drugs interact with ion channels in the cells of our heart and trigger heart rhythm disorders with potentially fatal consequences. Computational modeling can provide mechanistic insight into the onset and propagation of drug-induced arrhythmias, but the effect of drugs on the mechanical performance of the heart remains poorly understood. Here we establish a multiphysics framework that integrates the biochemical, electrical, and mechanical effects of drugs, from cellular excitation to cardiac contraction. For the example of the drug dofetilide, we show that drug concentrations of 5x and 8x increase the heart rate to 122 and 114 beats per minute, increase myofiber stretches by 5%, and decrease overall tissue relaxation by 6%. This results in inter-ventricular and atrial-ventricular dyssynchronies and changes in cardiac output by  $-2.5\%$  and  $+7\%$ . Our results emphasize the need for multiphysics modeling to better understand the mechanical implications of drug-induced arrhythmias. Knowing how different drug concentrations affect the performance of the heart has important clinical implications in drug safety evaluation and personalized medicine.

**Keywords** Cardiac mechanics · Cardiac electrophysiology · Drug-induced arrhythmia · Computational whole-heart modeling · Electro-mechanical coupling · Hemodynamic coupling

## 1 Motivation

All medications have side effects. Drug-induced ventricular arrhythmia and sudden cardiac death are rare but severe adverse events that should be avoided at all cost. Consequently, when a new drug is developed, the proarrhythmic potential of the new compound is a key concern. The current gold standard pharmacological pro-arrhythmic risk stratification combines in vitro experiments to quantify pharmacological blocking of specific cardiac ion channels, with electrocardiographic large animal experiments and clinical studies focusing on changes in tissue activation duration. Although these biomarkers show good sensitivity, they are

costly and have poor specificity, potentially blocking safe new drugs from ever reaching the market [1]. To develop novel and more accurate drug-induced arrhythmia biomarkers, multiphysics multiscale models mechanistically couple what a pharmacologist sees in a single cell experiment to what a physician sees in a clinical electrocardiogram [2]. As part of these efforts, our group has recently proposed an electrophysiological exposure-response simulator that integrates the interaction between multiple drug compounds and specific ionic currents at the cellular scale with the intrinsic cardiac anisotropic conductivity at the tissue scale and the transmural heterogeneity and tissue organization at the organ scale [3]. This framework allows us to conduct in silico drug trials for multiple drugs at various concentrations [4], providing risk categories that correlate well with reported drug-induced arrhythmia incidence [5]. Based on these results, we trained and validated a binary risk classifier that accurately predicts the critical pro-arrhythmic drug concentration [6,7]. From a clinical perspective however, a binary risk classification only provides a limited insight into the malignancy of the arrhythmic event. Dependent on the periodicity of the drug-induced arrhythmia, the cardiac output can increase, decrease or stay relatively constant. Consequently, short-duration non-sustained arrhythmogenicity can have multiple outcomes for

---

✉ E. Kuhl  
ekuhl@stanford.edu

<sup>1</sup> Department of Mechanical Engineering, Stanford University, Stanford, CA, USA

<sup>2</sup> Department of Biomechanical Engineering, Delft University of Technology, Delft, Netherlands

<sup>3</sup> Dassault Systemes Simulia Corporation, Johnston, RI, USA

<sup>4</sup> Department of Mechanical Engineering, Pontificia Universidad Catolica de Chile, Santiago, Chile

<sup>5</sup> Departments of Mechanical Engineering and Bioengineering, Stanford University, Stanford, CA, USA

the patient. In this study, we extend our framework to provide insights into the changing cardiac output of the heart at varying arrhythmogenic drug concentrations. More specifically, we use the electrophysiological activation sequence to drive biomechanical tissue contraction in the human heart and study the resulting hemodynamic effects on the whole-body cardiovascular circulation. Doing so, we compute a drug's pharmacological potential to impede efficient propulsion of blood through the heart chambers and the rest of the body. As such, we extend what a physician sees in a clinical electrocardiogram to what a patient feels and how likely they are to survive specific dosage-dependent drug-induced arrhythmia events.

## 2 Methods

### 2.1 Cardiac electrophysiology

We simulated the electrophysiological behavior of cardiac tissue using the monodomain model [8]. The main variable of the monodomain model is the transmembrane potential  $\phi$ , the difference between the intra- and extra-cellular potentials. The transmembrane potential is governed by a reaction-diffusion equation [9],

$$\dot{\phi} = \text{div}(\mathbf{D} \cdot \nabla \phi) + f^\phi, \quad (1)$$

where  $f^\phi$  are the ionic currents across the cell membrane and  $\mathbf{D}$  is the conductivity tensor,

$$\mathbf{D} = D^\parallel \mathbf{f} \otimes \mathbf{f} + D^\perp [\mathbf{I} - \mathbf{f} \otimes \mathbf{f}], \quad (2)$$

which we further decomposed into fast  $D^\parallel$  and slow  $D^\perp$  signal propagation parallel and perpendicular to the cardiac muscle fiber direction  $\mathbf{f}$ , where  $\mathbf{I}$  is the second-order unit tensor [10]. In general, the ionic currents  $f^\phi(\phi, \mathbf{q}(\phi); t)$  are functions of the transmembrane potential  $\phi$  and a set of state variables  $\mathbf{q}(\phi)$  [11,12], where the state variables themselves are governed by ordinary differential equations,  $\dot{\mathbf{q}} = \mathbf{g}(\phi, \mathbf{q}(\phi); t)$ . The number of currents and state variables determines the complexity of the model and varies for different cell types.

To simulate the electrophysiological behavior of the Purkinje fiber network, we chose the Stewart model for human Purkinje fiber cells [13]. A characteristic feature of this model is the automaticity of its action potential, which enables the cells to self-excite without an external stimulus. This model is based on 14 ionic currents

$$I = I_{\text{CaL}} + I_{\text{Na}} + I_{\text{Cab}} + I_{\text{Nab}} + I_{\text{Kr}} + I_{\text{Ks}} + I_{\text{K1}} + I_{\text{to}} + I_{\text{f}} + I_{\text{sus}} + I_{\text{NaK}} + I_{\text{pCa}} + I_{\text{pK}} + I_{\text{NaCa}} \quad (3)$$

that are defined through 20 state variables.

To study the spatiotemporal action potential evolution in the myocardium, we selected the O'Hara-Rudy model for human ventricular cardiomyocytes [14]. This model was developed based on a vast amount of human experimental data and includes description of key ionic currents for drug-induced arrhythmias. More specifically, the model is based on 15 ionic currents,

$$I = I_{\text{CaL}} + I_{\text{Na}} + I_{\text{CaNa}} + I_{\text{CaK}} + I_{\text{Cab}} + I_{\text{Nab}} + I_{\text{Kb}} + I_{\text{Kr}} + I_{\text{Ks}} + I_{\text{K1}} + I_{\text{to}} + I_{\text{NaK}} + I_{\text{pCa}} + I_{\text{NaCa,i}} + I_{\text{NaCa,ss}} \quad (4)$$

of which we replaced the fast sodium current  $I_{\text{Na}}$  of the original O'Hara-Rudy model with a modified fast sodium current of the ten Tusscher model [15] to model propagation in tissue scale simulations [16]. These 15 transmembrane ion currents are defined through a total of 39 state variables. To account for regional specificity, we reparametrized the cardiomyocyte cell model for three different cell types: endocardial, mid-wall, and epicardial cells [14].

We incorporated drug effects by blocking the currents of the pharmacologically affected ion channels on the Purkinje and cardiomyocyte cell membrane. Based on discrete experimental patch clamp measurements of the fractional ion channel block at various drug concentrations [17], we fitted a Hill-type equation

$$\beta = \frac{C^h}{IC_{50}^h + C^h}, \quad (5)$$

to describe fractional blockage  $\beta$  at any possible drug concentrations  $C$ . Here, the drug's concentration-specific ion channel block is completely described by two parameters: the Hill exponent  $h$  and the concentration  $IC_{50}$  required to achieve a 50% current block. Here we focused on the drug dofetilide, a selective  $I_{\text{Kr}}$  blocker, characterized by the experimentally estimated half maximal inhibitory concentration  $IC_{50,\text{Kr}} = 2.0 \text{ nM}$  and the Hill exponent  $h_{\text{Kr}} = 0.65$  [17]. These parameters are consistent with a prospective randomized controlled clinical trial studying the effect of dofetilide administration on QTc prolongation in healthy patients [5,18]. To apply the drug at a desired concentration  $C$ , we calculated the fractional blockage  $\beta_{\text{Kr}}$  and scaled the rapid delayed rectifier potassium ion channel conductance,

$$I_{\text{Kr}}^{\text{drug}} = [1 - \beta_{\text{Kr}}] I_{\text{Kr}} \quad (6)$$

by multiplying the baseline current  $I_{\text{Kr}}$  with the fractional blockage  $[1 - \beta_{\text{Kr}}]$ . We focused on  $I_{\text{Kr}}$  blockages of 75%, 80%, and 90% [19], which corresponds to effective therapeutic free plasma concentrations of 10.8 nM, 16.9 nM and

58.8 nM, or to concentrations of 5x, 8x, and 28x when normalized by the maximal effective free therapeutic plasma concentration of 2.0 nM [20].

To solve the governing Eqs. (1–6) we adopted the finite element software package Abaqus [21]. We exploited the structural similarities between the electrophysiological problem and a heat transfer problem with a non-linear heat source. We discretized the transmembrane potential as a nodal degree of freedom and the ionic currents and gating variables as internal variables [10]. Motivated by the small time step size to resolve the fast dynamics during the initial phase of the action potential, we adopted an explicit time integration scheme.

## 2.2 Cardiac mechanics

To model the mechanical behavior of cardiac tissue, we solved the equilibrium equations of Newton's law,

$$\text{div}(\boldsymbol{\sigma}) + \rho \mathbf{f}^\varphi = \mathbf{0} \quad \text{with} \quad \boldsymbol{\sigma} = \boldsymbol{\sigma}_{\text{pas}} + \boldsymbol{\sigma}_{\text{act}}, \quad (7)$$

where  $\boldsymbol{\sigma}$  is the Cauchy stress tensor that we additively decomposed into passive and active parts  $\boldsymbol{\sigma}_{\text{pas}}$  and  $\boldsymbol{\sigma}_{\text{act}}$ ,  $\rho$  is the material density and  $\mathbf{f}^\varphi$  is the body force per unit mass. We adopt the kinematics of finite deformation in terms of the deformation field  $\boldsymbol{\varphi}$ ,

$$\mathbf{F} = \nabla \boldsymbol{\varphi} \quad \text{and} \quad \mathbf{F} = \bar{\mathbf{F}} \cdot \mathbf{F}_{\text{vol}}, \quad (8)$$

where  $\mathbf{F}$  is the deformation gradient that we multiplicatively decomposed into a volumetric part,  $\mathbf{F}_{\text{vol}} = J^{1/3} \mathbf{I}$ , and an isochoric part,  $\bar{\mathbf{F}} = \mathbf{F} \cdot \mathbf{F}_{\text{vol}}^{-1} = J^{-1/3} \mathbf{F}$ , with  $J = \det(\mathbf{F})$  denoting the Jacobian. To characterize tissue stretch, we used the right Cauchy-Green deformation tensor,  $\mathbf{C} = \mathbf{F}^t \cdot \mathbf{F}$ , its isochoric counterpart,  $\bar{\mathbf{C}} = \bar{\mathbf{F}}^t \cdot \bar{\mathbf{F}} = J^{-2/3} \mathbf{C}$ , and its invariants,

$$\begin{aligned} \bar{I}_1 &= \bar{\mathbf{C}} : \mathbf{I} & \bar{I}_{4f} &= \bar{\mathbf{C}} : [\mathbf{f}_0 \otimes \mathbf{f}_0] \\ \bar{I}_{4fs} &= \bar{\mathbf{C}} : [\mathbf{f}_0 \otimes \mathbf{s}_0]^{\text{sym}} & \bar{I}_{4s} &= \bar{\mathbf{C}} : [\mathbf{s}_0 \otimes \mathbf{s}_0], \end{aligned} \quad (9)$$

where  $\mathbf{f}_0$  and  $\mathbf{s}_0$  denote the cardiac muscle fiber and sheet directions in the undeformed configuration.

We characterized the passive behavior of the tissue through a hyperelastic strain energy function,

$$\psi_{\text{pas}} = \psi_{\text{vol}} + \bar{\psi}_{\text{iso}} + \bar{\psi}_{\text{ani}}, \quad (10)$$

where  $\psi_{\text{pas}}$  denotes the passive strain energy that we additively decomposed into a volumetric part  $\psi_{\text{vol}}$  [22], an isotropic isochoric part  $\bar{\psi}_{\text{iso}}$ , and an anisotropic isochoric part  $\bar{\psi}_{\text{ani}}$  [23],

$$\psi_{\text{vol}} = \frac{1}{2d} [J^2 - 2 \ln J - 1]$$

$$\begin{aligned} \bar{\psi}_{\text{iso}} &= \frac{a}{2b} \exp(b [\bar{I}_1 - 3]) \\ \bar{\psi}_{\text{ani}} &= \frac{a_f}{2b_f} [\exp(b_f [\bar{I}_{4f} - 1]^2) - 1] \\ &\quad + \frac{a_s}{2b_s} [\exp(b_s [\bar{I}_{4s} - 1]^2) - 1] \\ &\quad + \frac{a_{fs}}{2b_{fs}} [\exp(b_{fs} \bar{I}_{4fs}^2) - 1]. \end{aligned} \quad (11)$$

Following the standard principles of thermodynamics, we expressed the passive Cauchy stress,

$$\boldsymbol{\sigma}_{\text{pas}} = \mathbf{F} \cdot \frac{2}{J} \frac{\partial \psi}{\partial \mathbf{C}} \cdot \mathbf{F}^t = \boldsymbol{\sigma}_{\text{vol}} + \boldsymbol{\sigma}_{\text{iso}} + \boldsymbol{\sigma}_{\text{ani}} \quad (12)$$

in terms of its volumetric, isotropic and anisotropic isochoric parts [24],

$$\begin{aligned} \boldsymbol{\sigma}_{\text{vol}} &= [J - 1/J]/d \mathbf{I} \\ \boldsymbol{\sigma}_{\text{iso}} &= a \exp(b [\bar{I}_1 - 3])/J \mathbf{B} : \mathbb{P} \\ \boldsymbol{\sigma}_{\text{ani}} &= 2a_f [\bar{I}_{4f} - 1] \exp(b_f [\bar{I}_{4f} - 1]^2)/J [\mathbf{f} \otimes \mathbf{f}] : \mathbb{P} \\ &\quad + 2a_s [\bar{I}_{4s} - 1] \exp(b_s [\bar{I}_{4s} - 1]^2)/J [\mathbf{s} \otimes \mathbf{s}] : \mathbb{P} \\ &\quad + 2a_{fs} \bar{I}_{4fs} \exp(b_{fs} \bar{I}_{4fs}^2)/J [\mathbf{f} \otimes \mathbf{s}]^{\text{sym}} : \mathbb{P}, \end{aligned} \quad (13)$$

where  $\mathbf{B} = \mathbf{F} \cdot \mathbf{F}^t$  is the left Cauchy Green deformation tensor,  $\mathbf{f} = \mathbf{F} \cdot \mathbf{f}_0$  and  $\mathbf{s} = \mathbf{F} \cdot \mathbf{s}_0$  are the deformed fiber and sheet directions,  $\mathbb{P} = \mathbb{I} - \frac{1}{3} \mathbf{I} \otimes \mathbf{I}$  is the fourth-order deviatoric projection tensor, and  $\mathbb{I}$  is the fourth-order unit tensor [25]. We described the active stress contribution using a time-varying elastance model [26]. We assumed that depolarization causes the inflow of calcium ions into the cells, and myocyte contraction. We also acknowledge the Frank-Starling effect, by introducing an active stress that depends on both the regional calcium concentration  $\text{Ca}^{2+}$  and on the sarcomere stretch state  $\lambda_f$ ,

$$\boldsymbol{\sigma}_{\text{act}} = T_{\text{act}}([\text{Ca}^{2+}], \lambda_f) [\mathbf{f} \otimes \mathbf{f} + \nu \mathbf{s} \otimes \mathbf{s}], \quad (14)$$

where  $\nu$  describes the active stress interaction between adjacent muscle fibers along the sheet direction  $\mathbf{s}$  [27].

We solved the governing Eqs. (7–14) within the finite element software package Abaqus using the heat transfer analogy between electrophysiology and temperature [21]. We set up a Fortran-based user-defined material subroutine to describe the Cauchy stress with respect to the deformation invariants, membrane potential, and time. We adopted all mechanical constitutive parameter values from our prior work [28].

## 2.3 Finite element implementation

The basis for our simulation is the Living Human Heart Model, an anatomically accurate four-chamber model of the healthy human heart [29,30]. The underlying anatomic

geometry is based on magnetic resonance imaging of a healthy, 30-year old, 50th percentile U.S. male [31]. Images were reconstructed from 0.75 mm thick slices using a medium soft-tissue kernel with retrospective electrocardiogram gating. Data acquisition and reconstruction were performed during 70% diastole. The resulting anatomically accurate model includes all four chambers, and the major vessels including the aorta, the pulmonary arteries and the superior vena cava. We prescribed the complex myocardial and atrial architecture of myofiber  $\mathbf{f}_0$  and sheet  $\mathbf{s}_0$  orientations using rule-based algorithms based on observations from histology and DT-MRI [28,32,33].

In this study, we neglected mechano-electrical feedback [34] and solved the electrophysiological and mechanical problem using a staggered approach. The balance between accuracy and computational cost with respect to element size and critical time step for the defined electrophysiological and mechanical problem leads to two different sets of spatiotemporal discretizations [35,36]. Consequently, we used two different meshes; one to solve the electrophysiological problem in both ventricles specifically and one to subsequently couple the electrophysiological results to the full heart model's mechanical behavior. For each case, we simulated five seconds without any drug administration followed by an additional five seconds of drug exposure to study the effect of dofetilide on the mechanical behavior and pump efficiency of the heart.

### 2.3.1 Electrophysiologica drug response

**Ventricular tissue model** Given our focus on drug-induced ventricular arrhythmogenesis and the fact that the atria are electrically isolated from the ventricles, we concentrated on electrophysiological drug effects in the ventricles. Motivated by the relationship between element size and critical time step size in explicit methods, we converted the ventricular geometry into a regular spatial discretization of cube elements with a constant edge length of 0.3 mm across the entire domain. This results in a discretization with 6,878,459 regular linear hexagonal finite elements, 7,519,918 nodes, and 268,259,901 internal variables. For the flux term, we included tissue anisotropy using the fiber definitions  $\mathbf{f}_0$  and assigned longitudinal and transverse conductivities  $D^{\parallel} = 0.090 \text{ mm}^2/\text{ms}$  and  $D^{\perp} = 0.012 \text{ mm}^2/\text{ms}$  [37]. For the source term, we employed a body flux subroutine to incorporate the ionic currents  $I_{\text{ion}}$  in the solid element formulation [21]. To account for and assign regional variations in cell type, we ran a series of Laplace problems using the finite element mesh with different essential boundary conditions [38]. From the solutions, we defined the different cell types across the wall, 20% of endocardial cells, 30% of mid wall cells, and 50% of epicardial cells. This arrangement ensures positive T-waves in the healthy baseline electrocardiogram [39].

**Purkinje network model** The inclusion of the Purkinje network is critical to model correct excitation patterns [9]. We created the network as a fractal tree that grows on the endocardial surface [40]. This resulted in a discretization with 39,772 linear cable elements, 39,842 nodes, and 795,440 internal variables. For these Purkinje fiber elements, we developed a linear user element with a discrete version of equation 1. We only connected the Purkinje network to the ventricular tissue at the terminals of the fractal tree [41]. For these connections, we used 3545 resistor elements with a resistance of  $1.78 \Omega\text{m}$ , i.e.,  $\chi = 140 \text{ mm}^{-1}$  and  $C_m = 0.01 \mu\text{F}/\text{mm}^2$  [37], between each endpoint of the network and the closest node of the ventricular mesh [42]. This allowed us to adopt distinct cellular models with different resting potentials for ventricular cells and Purkinje cells. Including resistor elements ensures a bi-directional conduction between Purkinje network and surrounding tissue. For the flux term, we set a conductivity of  $D = 3.0 \text{ mm}^2/\text{ms}$ .

**Electrocardiogram computation** To calculate pseudo electrocardiograms, at every point  $\mathbf{x} \in \mathcal{B}$  across the heart we projected the heart vector  $\nabla\phi$  onto the direction vector  $\nabla(1/||\mathbf{r}||)$  and integrated this projection across the entire cardiac domain  $\mathcal{B}$  [9,43],

$$\phi_e(\mathbf{x}_e) = - \int_{\mathcal{B}} \nabla\phi \cdot \nabla \frac{1}{||\mathbf{r}||} dV \quad \text{with} \quad \mathbf{r} = ||\mathbf{x}_e - \mathbf{x}||. \quad (15)$$

The vector  $\mathbf{r}$  points from current point  $\mathbf{x}$  to the electrode position  $\mathbf{x}_e$ . To mimic the recording of pre-cordial lead V3 in the clinical electrocardiogram, we placed the electrode 2 cm away from the left ventricular wall. This pre-cordial lead is commonly used to study T waves and QT intervals [44], which are critical to assess the risk of drug toxicity [45].

### 2.3.2 Mechanical drug response

**Electromechanical coupling** For the mechanical problem, a coarser spatial discretization suffices to compute accurate responses [29]. Therefore, we discretized the ventricles using 192,040 linear tetrahedral elements with a mean edge size of 2.5 mm and 44,182 nodes. Consequently, the electromechanical coupling required the interpolation of a three-dimensional 7,519,918 nodal temperature field to a three-dimensional 44,182 nodal temperature field. This was accomplished using Abaqus's temperature field interpolation functionality between dissimilar meshes in subsequent analyses [21]. The full heart mesh, including atria and proximal vasculature parts, comprised 76,282 nodes and 290,723 elements and local fiber- and sheet-orientation assignments. This discretization introduced 228,846 degrees of freedom for the vector-valued deformation. We constrained the heart kinematically through homogeneous Dirichlet boundary conditions at the outlets of the proximal vasculature [30]. We



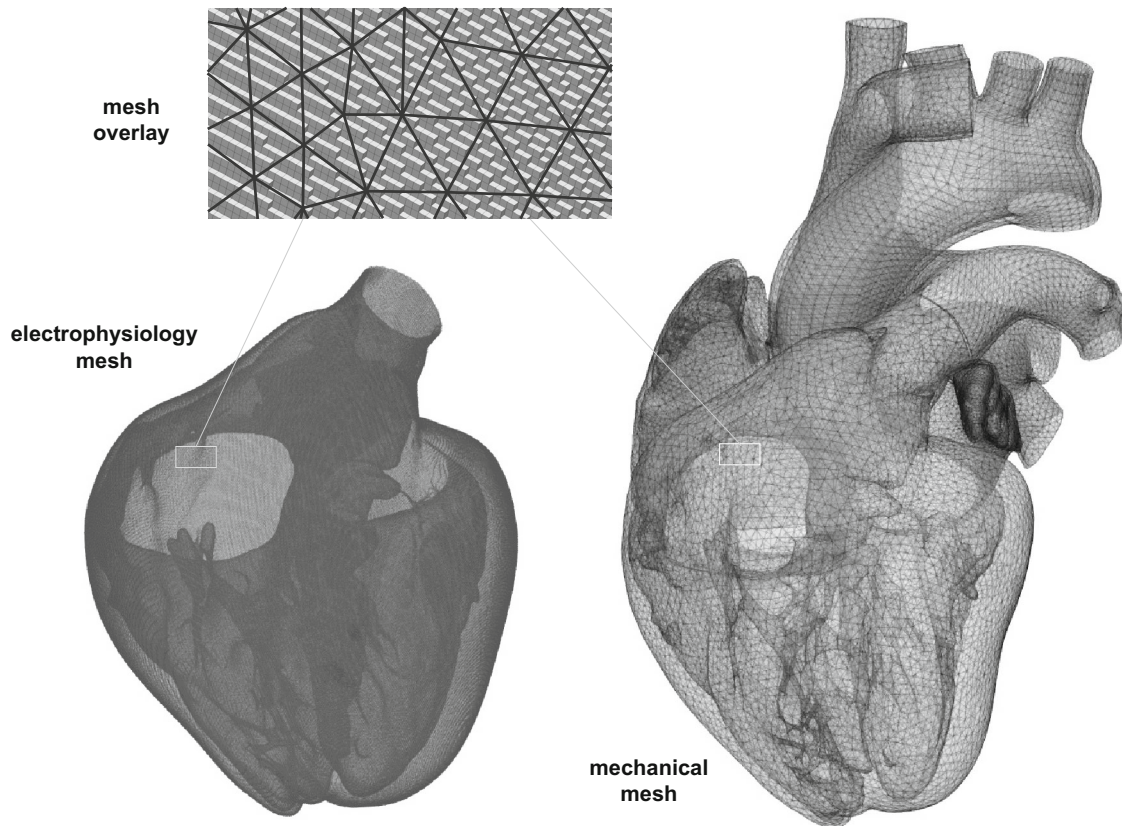


**Fig. 1** Spatial discretization to compute the electrophysiological and mechanical solution. A mismatch in required spatiotemporal discretization to solve the electrophysiological and mechanical problem leads to two different mesh sizes. To quantify the effects of the drug dofetilide on the activation sequence of the heart, we discretized the ventricles using 39,772 linear cable elements describing the Purkinje fibers and

6,878,459 regular linear hexagonal elements describing the myocardial tissue. Concomitantly, we computed the biomechanical behavior of the ventricles using a mesh consisting of 192,040 tetrahedral elements. We meshed the atria and proximal vasculature using 98,683 additional tetrahedral elements

described the atrial action potential, which is not explicitly simulated in our electrophysiological ventricular drug-exposure response simulator, using a physiological amplitude step function [46]. We reported quantitative myofiber stretches across the left and right ventricular wall according to the temporal median value and the 95% confidence interval.

**Coupling to cardiovascular circulation** In order to provide realistic loading conditions and hemodynamic boundary conditions for the atria and ventricles in the heart model, a closed-loop lumped parameter model was set up in Abaqus [29]. This lumped parameter model comprises the surface-based fluid cavity representation of the four chambers and additional unit cube fluid cavities representing the arterial and venous systemic and pulmonary circulation. We modeled the mitral/tricuspid valve, the aortic/pulmonary valve, and the systemic/pulmonary resistance flow resistances between these chambers using fluid exchange resistors. We incorporated chamber-specific structural compliances of the additional arterial, venous, and pulmonary chambers using capacitors on one free wall of the unit cube fluid cavities.

Since we deduced the geometry of the heart at 70% diastole with the heart already hemodynamically loaded, we estimated the in vivo stress state at the beginning of the simulation using an inverse prestressing method [47,48].

**Pressure-volume loops and cardiac output** The pressure and volume in the left and right ventricle was computed using the hemodynamic fluid-cavity definition of both chambers in Abaqus. From these measurements, the pressure-volume loops in both ventricles were extracted. We computed the average stroke volume using the last three simulated dynamically changing pressure volume loops. The average case-specific heart rate was computed based on the average time difference between the last three strokes. Similarly, the time difference between the maximum left and right ventricular contraction was extracted from the last three ventricle-specific contraction sequences. The instantaneous left and right ventricular cardiac output was computed based on the outflow from the left and right ventricular fluid cavity. A 2-second rolling average of this instantaneous outflow expressed as average outflow per minute provided a more

descriptive insight on how the cardiac output changes with respect to different administered dofetilide drug concentrations.

### 3 Results

#### 3.1 Electrophysiological drug effects

Figure 2 and the Supplementary Video show the different activation patterns at healthy baseline, and dofetilide 5x, dofetilide 8x and dofetilide 28x administration. These cases correspond to 0%, 75%, 80%, and 90% block of the  $I_{kr}$  ion channel current. For the baseline case, where no drug is applied, we observe a regular activation sequence that repeats itself ten times in the electrocardiogram. The QRS complex, which represents the fast depolarization driven by the Purkinje network, is preceded by a P wave, which highlights the atrial activation.

By blocking the  $I_{kr}$  current 75%, induced by administration of 5x dofetilide five seconds after drug-free pacing, we see a disruption in the periodic rhythm of the ventricles, leading to arrhythmogenesis that shares features of torsades de pointes. The first electrophysiological depolarization wave after drug administration is still driven by the Purkinje network, as shown in the first snapshot, followed by a delay in repolarization, which leads to a secondary activation caused by early afterdepolarizations in a group of midwall cells.

The case of 80% block of  $I_{kr}$  induced by 8x dofetilide also shows drug-induced arrhythmogenicity, which is qualitatively similar to the 75% block case. However, the differences in both activation patterns and electrocardiogram recordings highlight the chaotic nature of the arrhythmia, where only a small perturbation in  $I_{kr}$  block leads to a significantly different temporal evolution of the transmembrane potential. At 5x dofetilide, the left and right ventricle first get activated from base to apex and subsequently from right to left ventricle. At 8x dofetilide administration, the depolarization wave evolves towards a mostly baso-apical ventricular activation sequence, where left ventricular depolarization slightly precedes right ventricular depolarization.

The final case of 90% block of  $I_{kr}$  caused by 28x dofetilide shows an arrhythmic event that is closer to ventricular fibrillation, as there are multiple spiral waves driving contractile tissue activation. This chaotic behavior is reflected in the electrocardiogram, where the QRS complexes during the arrhythmia are less defined, with a lower amplitude.

#### 3.2 Mechanical drug effects

Figure 3 and the Supplementary Video highlight the effect that different drug concentrations have on the time sequence of regional myocyte activation over time. The shown snap-

shots correspond to the time points from Fig. 2 with a delay of 50 ms (to showcase the locally induced myocardial contraction following a depolarization wave). Figure 4 showcases the left and right ventricular myofiber stretch evolution over time during the five seconds after drug administration. For the baseline no-drug case, the orchestrated depolarization wave of both the left and right ventricle from apex to base causes the ventricles to contract collectively, pushing the blood volume out to the systemic and pulmonary circulation in one cooperative squeeze. More specifically, the myofiber stretches during maximum contraction measure 0.766 (95% CI 0.704–0.828) and 0.671 (95% CI 0.634–0.797) for the left and right ventricles. Moreover, the myocardium is fully relaxed during the atrial contraction, allowing an optimal additional filling of the ventricles during the atrial kick. The myofiber stretches at full relaxation amount to 1.070 (95% CI 1.021–1.134) and 1.055 (95% CI 0.997–1.136) for the left and right ventricles. The myofiber contraction and relaxation remain in complete sync with an average absolute time difference of 25 ms between maximum left and right ventricular contraction. For the left ventricle, we compute minimum and maximum myofiber stretches of 0.704 and 1.139.

The 5x dofetilide-induced arrhythmogenicity leads to dyssynchronous myocardial contraction and relaxation patterns within the ventricles. Consequently, the myocardial tissue is in active contraction and passive tension at the same time, as can be seen from the wider shaded regions of myofiber stretch variability in Fig. 4. In more detail, for dofetilide 5x we compute left and right ventricular myofiber stretches of 0.776 (95% CI 0.730–0.837) and 0.689 (95% CI 0.642–0.804) at maximum contraction and myofiber stretches of 1.030 (95% CI 0.967–1.099) and 0.990 (95% CI 0.898–1.074) at maximum relaxation. The drug-induced torsadogenic activation sequence leads to a general right-left ventricular contraction dyssynchrony, during which the right ventricle contracts on average 117 ms prior to the left ventricle. Administration of 5x dofetilide leads to minimum and maximum left ventricular myofiber stretches of 0.710 and 1.208.

The mechanical effects of 8x dofetilide administration are similar to 5x dofetilide, however an important difference between both cases can be found in dyssynchrony. In contrast to 5x dofetilide, upon 8x dofetilide administration both left and right ventricular contraction remain mostly synchronized. We compute an average 25 ms time difference between left and right ventricular peak contraction, which agrees with the no-drug baseline case. Similar to 5x dofetilide, the left and right ventricular myofiber stretches after 8x dofetilide administration amount to 0.772 (95% CI 0.712–0.845) and 0.686 (95% CI 0.639–0.837) at maximum contraction, and 1.007 (95% CI 0.943–1.136) and 1.016 (95% CI 0.802–1.123) at maximum relaxation. 8x dofetilide affects the minimum and maximum left ventricular myofiber stretches measuring 0.712 and 1.187. For both 5x and 8x dofetilide administra-



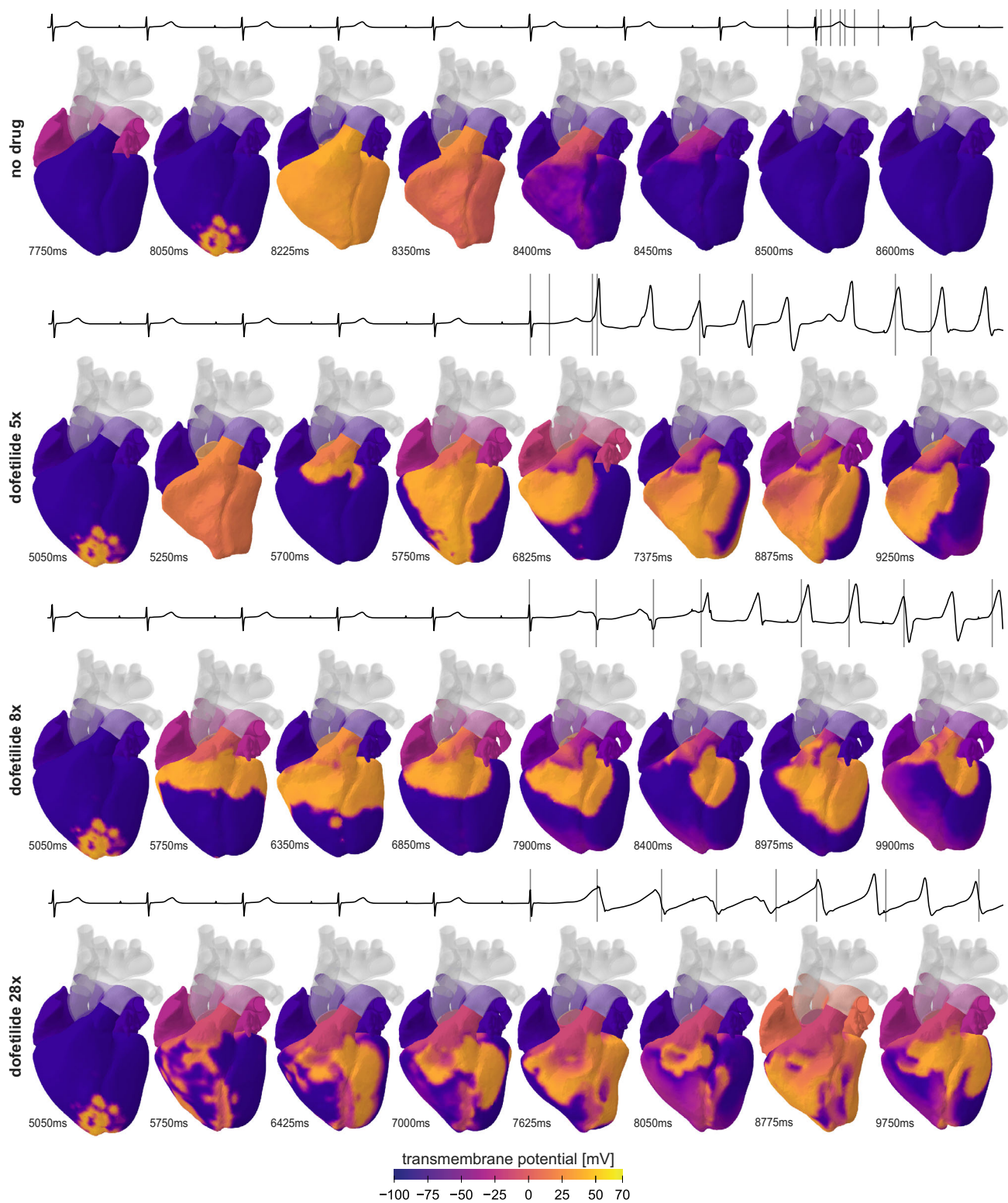


**Fig. 2** Time evolution of the transmembrane potential for different concentrations of dofetilide. Snapshots are taken at different timepoints for different cases of drug-induced  $I_{K_r}$  channel block, showcasing the contractile and relaxing deformation in correspondence to the color-plotted

electrical activation pattern in the heart. At the top of each row, the computed electrocardiogram signal is shown in black, where the grey vertical lines depict the showcased snapshots for each specific case

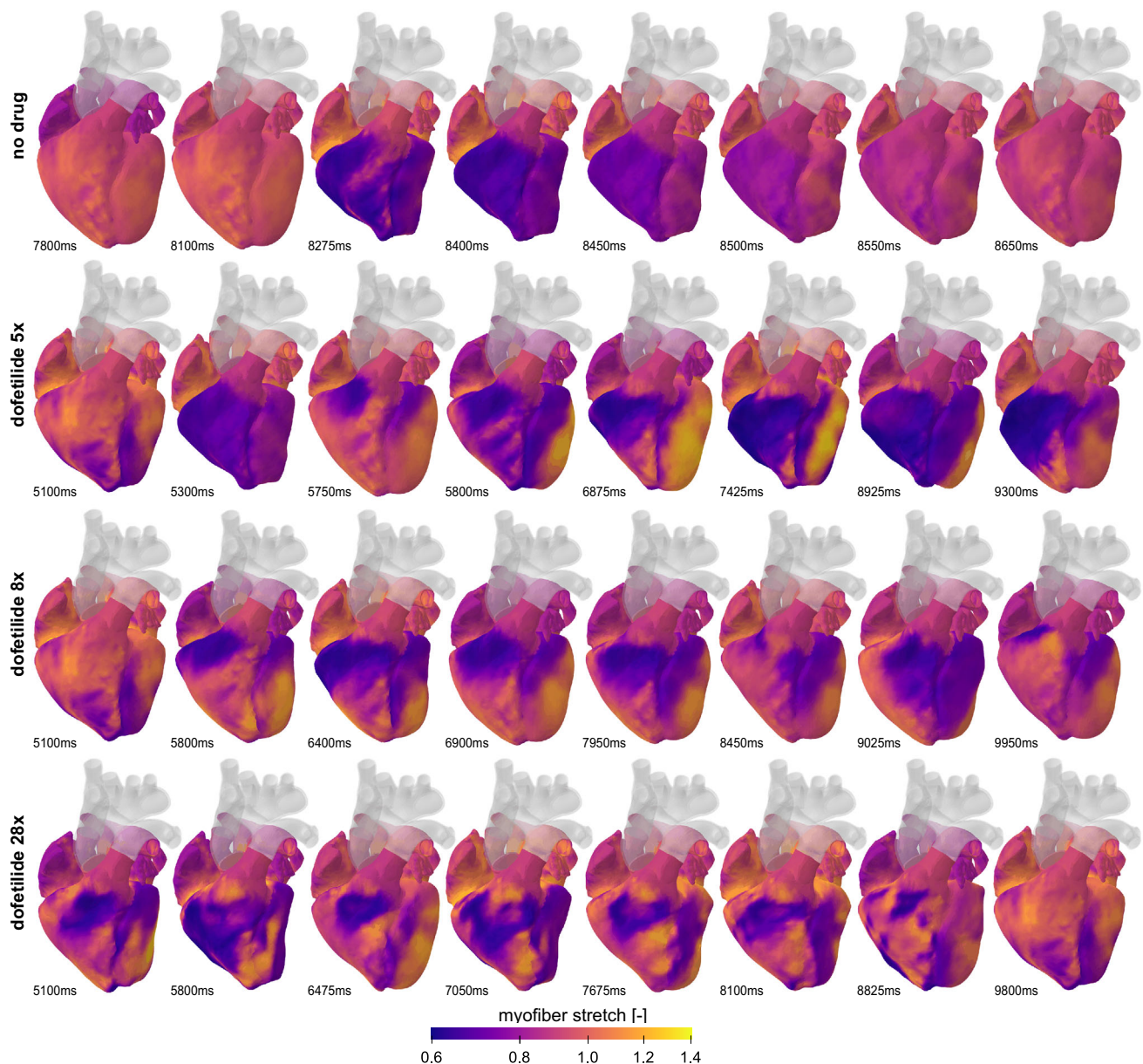


**Fig. 3** Spatiotemporal evolution of the myofiber stretch for different concentrations of dofetilide. Snapshots are taken at different timepoints for each case, showcasing the effect that blocking of the  $I_{Kr}$  channel, in

correspondence to different administered concentrations of dofetilide, has on the spatiotemporal contraction of the heart

tion, the maximum myofiber stretches are approximately 5% higher compared to the baseline no-drug case, and typically occur just prior to overall ventricular contraction. This effect arises from the partial contraction of the myocardial tissue during the interventricular pressure buildup phase, causing the tissue that is not activated yet to stretch beyond the baseline physiological stretch range. Concomitantly, the tissue does not properly relax in between contraction waves, leading to 6% lower relaxation stretch compared to the healthy baseline case. At the same time, the minimum left ventricu-

lar myofiber stretches at 5x and 8x dofetilide administration remain relatively comparable to the no-drug baseline case, showcasing the contractile capacity of the tissue is not heavily compromised.

Upon 28x dofetilide administration, the spatiotemporal stretch patterns in Fig. 3 are completely irregular, as can be expected from ventricular fibrillation. Consequently, little synchronicity in ventricular contraction and relaxation remains as can be seen from the large shaded temporal myofiber stretch variability shown in Fig. 4. The left and

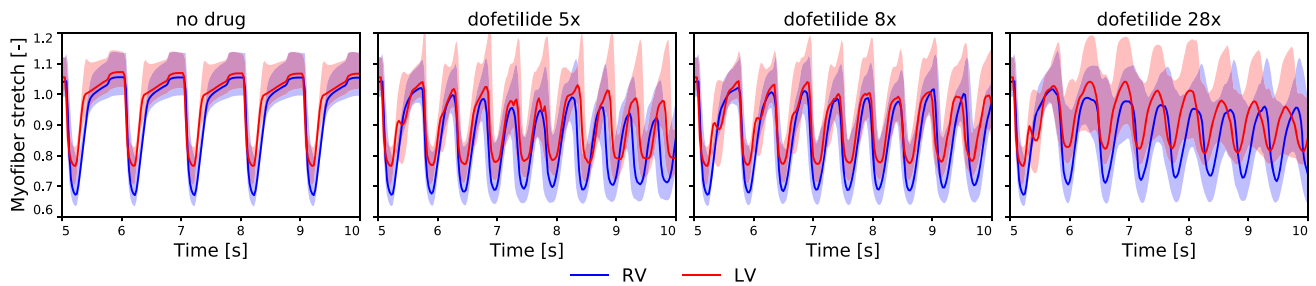


**Fig. 4** Time evolution of the left and right ventricular myofiber stretch for different concentrations of dofetilide. The temporal myofiber stretch evolution is shown for the left (red) and right ventricle (blue) for different administered concentrations of dofetilide. The solid lines showcase

the temporal median myofiber stretch value for each respective ventricle whilst the transparent shaded regions represent the ventricle-specific 95% myofiber stretch confidence intervals

right ventricular myofiber stretches amount to 0.807 (95% CI 0.768–1.026) and 0.716 (95% CI 0.649–0.981) during maximum contraction and 1.014 (95% CI 0.894–1.178) and 0.977 (95% CI 0.854–1.092) during maximum tissue relaxation. We compute maximum contractile myofiber stretches of 0.767 and maximum relaxing myofiber stretches of 1.179 in the left ventricle upon 28x dofetilide administration. It should be noted that periodicity in overall ventricular contraction-relaxation starts to fade at this drug concentration, showcased by the smaller amplitude of the median temporal myofiber stretch evolution and the minimum left ventricular myofiber stretches remaining relatively constant around 0.770–0.800 during the last three seconds. During the 28x dofetilide-induced ventricular fibrillation, the right-left ventricular dyssynchrony rises to a 92 ms time difference between left and right ventricular peak contraction. Similar to the 5x and 8x dofetilide cases, the maximum relaxed myofiber stretches are approximately 4% higher compared to the baseline case, whilst the median relaxed myofiber stretches are up to 5% smaller. Interestingly, at this drug concentration, we start seeing a compromised contractile capacity of the tissue with left ventricular maximum contractile myofiber stretches that are approximately 8% weaker, and left ventricular median contractile myofiber stretches that are approximately 5% weaker compared to the no-drug baseline case.

Overall, the myofiber stretch variability amounts to a temporally averaged standard deviation of 0.118, 0.114, 0.133 for dofetilide 5x, 8x and 28x administration. Compared to the no-drug baseline averaged myofiber stretch variability of 0.066, it can be seen how dofetilide affects an effective synchronized contraction of both ventricles, and leads to decreasing cardiac pumping efficiency.

This decreasing cardiac pump efficiency is shown in more detail with respect to the overall cardiovascular circulation in Fig. 5. The no-drug baseline pressure-volume loop for the left and right ventricle is shown in the left column. When no drug is administered the stroke volume remains constant at 72 ml. At 5x dofetilide administration, the stroke volume

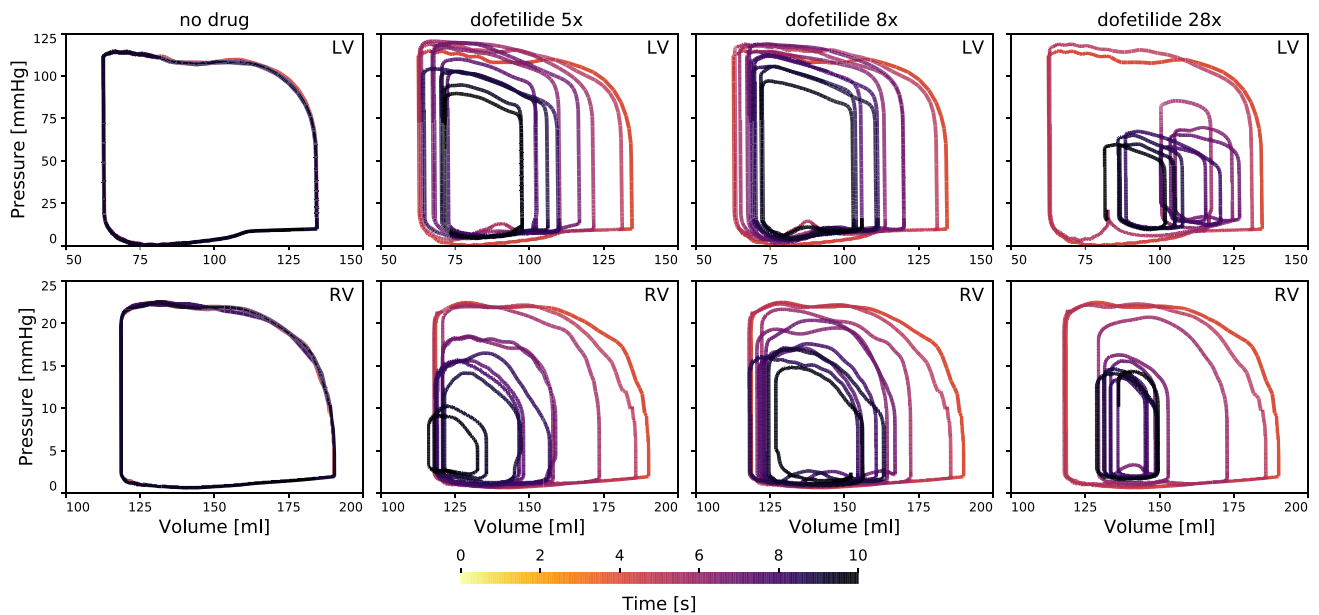
drops to 29 ml and 20 ml for the left and right ventricle. This stroke volume change is mostly caused by a drop in the end-diastolic volume, whilst the end-systolic volume stays approximately the same. The average arrhythmic heart rate after 5x dofetilide administration increases to 123 bpm. At a 80%  $I_{K_r}$  channel block induced by a 8x dofetilide administration, the stroke volume drops from 72 ml to 35 ml for both ventricles. Again, the drop in stroke volume is mostly caused by a smaller end-diastolic volume, whilst the end-systolic volume stays approximately constant. Dofetilide 8x causes the average arrhythmic heart rate to increase to 114 bpm. At a dofetilide administration of 28x, the stroke volume drops to 20 ml for the left ventricle and to 17 ml for the right ventricle. In this case, the drop in stroke volume is caused by both a decrease in the end diastolic volume and an increase in the end-systolic volume. The average arrhythmic heart rate increases to 109 bpm.

Figure 6 quantifies the combined effect of drug-induced changing heart rates and stroke volumes on the instantaneous and average cardiac output, denoted by a dotted and solid line. The cardiac outputs for the left and right ventricle are highlighted in red and blue. Shown here, 5x dofetilide administration leads to a +5% increase and a –10% decrease in the cardiac output for the left and right ventricle. For 8x dofetilide administration, the cardiac output has moderately increased after 5 seconds of drug exposure. More specifically, the left and right ventricular cardiac output increased +11% and +3% compared to the baseline cardiac output with no drug exposure. A 28x dofetilide administration causes a severe –46% and –64% decrease in left and right ventricular cardiac output.

## 4 Discussion

Many drugs—not just cardiac drugs—can have serious side effects. One of the most dangerous side effects entails the development of cardiac arrhythmias. More specifically, the





**Fig. 5** The pharmacological effects of dofetilide on the ventricular pressure-volume loops. Pressure-volume loops showcase the efficiency and frequency of heart contraction for each studied case. For the no-drug case, the pressure-volume loop remains the same. For a 75%  $I_{K_r}$  channel block (dofetilide 5x), the end-diastolic volume decreases significantly

and fluctuates whilst the heart rate increases. For a 80%  $I_{K_r}$  channel block (dofetilide 8x), the end-diastolic volume drops moderately and the heart rate increases. For a 90%  $I_{K_r}$  channel block (dofetilide 28x), the end-diastolic volume drops significantly and the end-systolic volumes increase for both ventricles whilst the heart rate increases

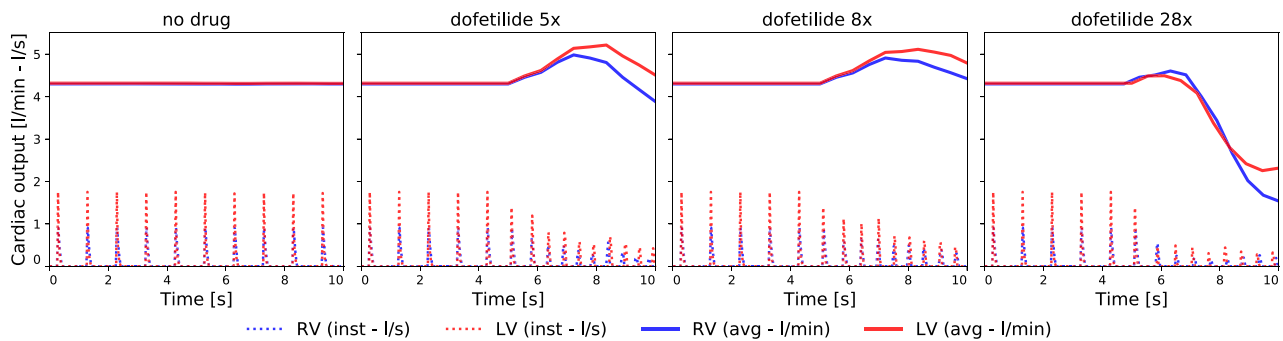


**Fig. 6** The pharmacological effects of dofetilide on the cardiac output. Cardiac output for the left ventricle (LV - red) and right ventricle (RV - blue) expressed instantaneously (dotted line - l/s) and as a 2-second

rolling average (solid line - l/min) for the normal case (left column), the mild case (middle column) and the severe case (right column)

development of torsades de pointes—a specific type of polymorphic ventricular tachycardia characterized by a gradual change in amplitude and twisting of the QRS complexes around an isoelectric line on the electrocardiogram [49]—can be especially lethal. Torsades de pointes are often transient but can, in severe cases, lead to ventricular fibrillation causing myocardial damage and even sudden cardiac death. Given its often short-termed episodic nature, most torsadogenic episodes remain under the radar [50,51], which leads to limited knowledge on the clinical behavior of the heart during such episodes. When picked up, the clinical evidence of these arrhythmia typically confines itself to electrocar-

diogram recordings. Pressure-volume loop measurements or flow measurements within a clinical setting are therefore typically unavailable. In this work, we use computational modeling to gather otherwise unattainable insights into the mechanical behavior of the human heart during drug-induced ventricular arrhythmogenic episodes.

To understand the genesis and development of drug-induced ventricular arrhythmia, cardiac electrophysiology needs to represent both the fast ionic subcellular mechanisms and the slower spatiotemporal cell-tissue-organ scale diffusion process in one and the same framework. To provide accurate physiological outputs and compute potential spi-

ral wave formation, we need a fine-scaled spatio-temporal discretization of the computational domain [35]. Cardiac deformation, however, is governed by smoother spatial and slower temporal scales. This implies that we can solve the mechanical balance equations with a coarser spatio-temporal discretization of the computational domain [36]. Given this mismatch in required spatio-temporal discretization and the exponential dependence of computation time on the number of degrees of freedom [52], we adopted up a unidirectional forward electromechanical coupling framework: We first computed the electrical propagation of the action potential through the ventricles using a fine-resolution exposure-response simulator [8], and then solve the biomechanical contraction of the cardiac tissue driven by the transmembrane potential. Since the contractility of the tissue is critically affected by pre-load and after-load conditions [53], we incorporated an active tension law that depends on the local and temporal sarcomere stretch state  $\lambda_f$  and coupled the electromechanical heart model to a realistic zero-dimensional surrogate lumped parameter network model of the cardiovascular circulation.

We successfully build an electrophysiological model that inherently captures the regional specificity of the ventricular myocardium and probes the dynamic interplay of its endocardial, midwall, epicardial, and Purkinje cells [3]. By extending this model with the dose-dependent effect of dofetilide on the transmembrane ion channel currents, we developed a mechanistic exposure-response simulator that is able to predict the three-dimensional excitation profiles and electrocardiogram recordings shown in Fig. 2. The *in silico* predicted dose-dependent torsadogenic risk of dofetilide agrees favorably with clinical and experimental findings [4,8]. By extending this multiscale framework to a multi-physics framework taking into account the mechanical behavior of the heart and its hemodynamic interaction with the surrounding cardiovascular circulation, we are now able to compute the pharmacological effects that different dosages of dofetilide have on the temporal mechanical behavior of myocardial tissue, as showcased in Figs. 3 and 4. Studying the pharmacological effects of different dosages of dofetilide on cardiac pump efficiency involves a complex interplay between regional tissue de- and repolarization, regional tissue contraction and relaxation, and continuously changing hemodynamic loading conditions through the heart's connection with the surrounding cardiovascular circulation. Therefore, we can only fully appreciate these effects by concomitantly studying the myofiber stretch state in Fig. 4, the pressure-volume loops depicted in Fig. 5 and the corresponding cardiac output in Fig. 6.

For the no-drug baseline case, both ventricles push out the blood in one cooperative synchronized contraction, followed by an extended relaxation phase allowing for atrial blood to refill the ventricle during early diastole and the atrial kick at end diastole. The myofiber stretches cooperatively

switch between a contractile and relaxing state, showcased by the low shaded temporal myofiber stretch variability in Fig. 4. These computed temporal myofiber stretch evolutions are in line with clinical observations for non-diseased human hearts, measured with both ultrasound and magnetic resonance imaging techniques [54–57]. Naturally, the corresponding pressure-volume loops and cardiac output remain constant.

Upon 5x dofetilide administration, the resulting torsadogenic activation sequence causes an important left-right ventricular contractility dyssynchrony. Immediately after drug administration, the left ventricular contraction starts to trail the right ventricular contraction. Additionally, the drug-induced torsadogenic swirling electrophysiological activation sequence drives the heart rate up to 123 bpm, which causes the ventricles to contract twice before the atria contract. Consequently, the passive atrial-ventricular filling time is significantly shortened, leading to a decreased mean myofiber stretch state during tissue relaxation in Fig. 4 and a drop in the left and right ventricular end-diastolic volumes in Fig. 5. The corresponding drop in the stroke volume leads to the decreasing instantaneous cardiac output showcased in Fig. 6. The increased heart rate also causes an important dyssynchrony between the atrial kick and the ventricular filling phase, further affecting efficient diastolic ventricular filling and decreasing the end diastolic volume. Initially, the atrial kick trails the ventricular contraction, however at specific timepoints within the simulated five-second drug administration timeframe, this dyssynchrony temporarily catches up, as can be appreciated from the fluctuating end diastolic volume evolution in Fig. 5. Interestingly, the decreased cardiac output is, at least initially, counterbalanced by the increased heart rate, which partially recovers the expected decrease in cardiac output in Fig. 6. For 8x dofetilide (80%  $I_{K_r}$  block), we see a similar combined effect of heart rate and ventricular filling. However, in this case, the torsadogenic activation sequence does not cause a strong left-right ventricular contraction dyssynchrony. Additionally, a heart rate of 114bpm leads to an atrial kick that leads the ventricular contraction, eventually becoming completely out of phase with the ventricular filling phase at the end of the five second simulated timeframe. This explains the gradual drop in stroke volume in Fig. 5. For 5x and 8x dofetilide administration, differences in cardiac output in Fig. 6 result from dose-dependent interventricular and atrial-ventricular dyssynchronies. Our results showcase a decreased and increased cardiac output for 5x dofetilide and 8x dofetilide, highlighting how higher arrhythmogenic drug concentration can impact the cardiac output in a non-intuitive way. Even though the 5x and 8x dofetilide induced arrhythmogenesis affects the cardiac output, the depolarization waves swirling around the ventricles still lead to a somewhat temporally structured contraction of the whole ventricle. The



resulting active force build up still leads to a decent contraction of the full ventricle, leading to end-systolic volumes that are only slightly larger than for the baseline no-drug case.

For the 28x dofetilide case however, the completely chaotic depolarization patterns no longer lead to a synchronous contraction, as can be seen by the large myofiber stretch variability through the whole arrhythmogenic episode in Fig. 4. As a result, both the left and right ventricular end-systolic volumes are considerably larger than normal. At the same time, the small re-entrant waves that flicker around the heart also strongly impact the diastolic filling time, leading to decreased end-diastolic volumes. The resulting decrease in stroke volume is so large that the resulting cardiac output in Fig. 6 drops significantly. Therefore, the risk for sudden cardiac death at 28x dofetilide administration can be expected to be significantly higher than for 5x and 8x dofetilide-induced arrhythmia episodes.

Apart from a more mechanistic sudden cardiac death risk stratification, our framework also gives important insights into drug-induced arrhythmogenic overstretching of the tissue. The tissue stretch state is believed to play an important role in pathophysiological growth and remodeling processes [28]. Compared to the no-drug baseline case, each drug-induced arrhythmogenic episode showcased increased myofiber stretches in Fig. 4. Additionally, at 28x dofetilide, the contractile capacity of the ventricles also got affected by the chaotic electromechanical depolarization and contraction patterns. As such, it can be appreciated that our framework provides both acute and chronic mechanistic insights into heart health during and after drug-induced arrhythmogenesis.

Our study provides valuable insights into the simultaneous pro-arrhythmic simultaneous pro-arrhythmic and inotropic liabilities of pharmacological therapies. We used the well-established O'Hara Rudy model for describing the electrophysiological behavior of the ventricular cardiomyocytes. This model was developed, calibrated and validated based on a vast amount of rate- and drug-dependent cellular electrophysiology experiments on undiseased human ventricular tissue samples [14]. The O'Hara Rudy model also serves as the consensus base model for the Comprehensive in Vitro Proarrhythmia Assay initiative established to develop a new paradigm for assessing proarrhythmic risk [58,59]. Despite its use as the consensus base model, novel updates to this model have recently been proposed which report dynamic drug- $I_{Kr}$  interactions and a re-assessment of the myocardial pro-arrhythmic sensitivity to  $I_{Kr}$  blockage [60,61], sex differences in drug-sensitive cardiomyocyte ion channel current densities [7], and apico-basal heterogeneity in the slow delayed rectifying potassium channel conductance [62]. These aspects might affect the critical drug concentration at which arrhythmia start developing in this study. Subsequently, we used a unidirectional excitation-

contraction model that takes into account myocardial preload and a critical depolarization threshold. It has recently been shown that two-way electromechanical coupling can partially mitigate the action potential duration induced by dofetilide, raising the critical concentration inducing early afterdepolarization onset [53]. Further model development providing a bidirectional coupling between human electrophysiology and active tension generation [34,63,64] will allow us to implement more detailed active tension generation models that take into account calcium dynamics, actin-myosin crossbridge cycling transition states and force-frequency responses. Importantly, these coupled models need to remain computationally tractable to be able to compute multiple serial heart beats and potential steady state outcomes. This is a challenging endeavor given the very stiff system of ordinary differential equations for the electrophysiology problem and the amount of state dependent variables in the contraction-excitation coupling, that can require up to 40x2400 CPU hours for simulating one heart cycle, even in a semi-implicit, operator splitted, MPI optimized framework [65]. Future work therefore also needs to study the sensitivity of inotropic whole body level results (e.g. end-diastolic and -systolic volumes, ventricular and atrial dyssynchrony, tachycardia) on the biophysical details of the underlying cellular models, and whether or not (potentially machine learning-based) reduced order models can speed up these computations [66–69].

## 5 Conclusion

This study provides a human-based multiscale and multi-physics mechanistic framework that couples the effect that a drug has on one singular ion channel down at the subcellular level all the way up to a changing cardiovascular circulation at the whole body level. The developed framework provides a granular insight in malignancy of concentration-dependent drug-induced ventricular arrhythmia. Our simulations extend the binary pro-arrhythmic risk classification paradigm for different drug concentrations to an assessment of arrhythmia-severity in light of clinical output metrics as pressure-volume loops and cardiac output. Here, we showed the clinical differences between three drug-induced arrhythmic episodes which results from the fine balance between electrophysiological action potential duration and depolarization times on the one hand and the contractile behavior of the myocardial tissue combined with the contraction of the atria and the connection to the surrounding cardiovascular circulation on the other hand.

**Supplementary Information** The online version contains supplementary material available at <https://doi.org/10.1007/s00466-022-02146-1>.

**Acknowledgements** This work used the Extreme Science and Engineering Discovery Environment (XSEDE) project TG-MSS170033 supported by the National Science Foundation Grant Number ACI-1548562, by a Belgian American Education Foundation Postdoctoral Research Fellowship, a Stanford Bio-X IIP Seed Grant, and the National Institutes of Health Grant R01HL131975.

## References

- Sager PT (2008) Key clinical considerations for demonstrating the utility of preclinical models to predict clinical drug-induced torsades de pointes. *Br J Pharmacol* 154:1544–1549
- Chabiniok R, Wang V, Hadjicharalambous M, Asner L, Lee J, Sermesant M, Kuhl E, Young A, Moireau P, Nash M, Chapelle D, Nordsletten DA (2016) Multiphysics and multiscale modeling, data-model fusion and integration of organ physiology in the clinic: ventricular cardiac mechanics. *Interface Focus* 6:20150083
- Sahli Costabal F, Yao J, Kuhl E (2018) Predicting drug-induced arrhythmias by multiscale modeling. *Int J Numer Methods Biomed Eng* 34(5):e2964
- Sahli Costabal F, Seo K, Ashley E, Kuhl E (2020) Classifying drugs by their arrhythmogenic risk using machine learning. *Biophys J* 118(5):1165–1176
- Sahli Costabal F, Matsuno K, Yao J, Perdikaris P, Kuhl E (2019) Machine learning in drug development: characterizing the effect of 30 drugs on the QT interval using Gaussian Process regression, sensitivity analysis, and uncertainty quantification. *Comput Methods Appl Mech Eng* 348:313–333
- Sahli Costabal F, Perdikaris P, Kuhl E, Hurtado DE (2020) Multifidelity classification using Gaussian processes: accelerating the prediction of large-scale computational models. *Comput Methods Appl Mech Eng* 357:112602
- Peirlinck M, Sahli Costabal F, Kuhl E (2021) Sex differences in drug-induced arrhythmogenesis. *Front Physiol* 12(1245):708435
- Sahli Costabal F, Yao J, Kuhl E (2018) Predicting the cardiac toxicity of drugs using a novel multiscale exposure-response simulator. *Comput Methods Biomech Biomed Eng* 21(3):232–246
- Krishnamoorthi S, Perotti LE, Borgstrom NP, Ajiola O, Aa Frid, Ponnaluri AV, Weiss JN, Qu Z, Klug WS, Ennis DB, Garfinkel A (2014) Simulation methods and validation criteria for modeling cardiac ventricular electrophysiology. *PLoS ONE* 9(12):e114494
- Göktepe S, Kuhl E (2009) Computational modeling of cardiac electrophysiology: a novel finite element approach. *Int J Numer Meth Eng* 79(2):156–178
- Lee LC, Sundnes J, Genet M, Wenk JF, Wall ST (2016) An integrated electromechanical-growth heart model for simulating cardiac therapies. *Biomech Model Mechanobiol* 15(4):791–803
- Wong J, Göktepe S, Kuhl E (2013) Computational modeling of chemo-electro-mechanical coupling: a novel implicit monolithic finite element approach. *Int J Numer Methods Biomed Eng* 29:1104–1133
- Stewart P, Aslanidi OV, Noble D, Noble PJ, Boyett MR, Zhang H (2009) Mathematical models of the electrical action potential of Purkinje fibre cells. *Philos Trans Math Phys Eng Sci* 367(1896):2225–2255
- O Hara T, Virág L, Varró A, Rudy Y (2011) Simulation of the undiseased human cardiac ventricular action potential: model formulation and experimental validation. *PLoS Comput Biol* 7(5):e1002061
- ten Tusscher KH, Noble D, Noble PJ, Panfilov AV (2004) A model for human ventricular tissue. *Am J Physiol Heart Circ Physiol* 286(4):H1573–89
- Priest JR, Gawad C, Kahlig KM, Yu JK, OHara T, Boyle PM, Rajamani S, Clark MJ, Garcia STK, Ceresnak S, Harris J, Boyle S, Dewey FE, Malloy-Walton L, Dunn K, Grove M, Perez MV, Neff NF, Chen R, Maeda K, Dubin A, Belardinelli L, West J, Antolik C, Macaya D, Quertermous T, Trayanova NA, Quake SR (2016) Early somatic mosaicism is a rare cause of long-QT syndrome. *Proc Natl Acad Sci* 113(41):115550–11560
- Crumb W, Vicente J, Johannesen L, Strauss D (2016) An evaluation of 30 clinical drugs against the comprehensive in vitro proarrhythmia assay (CiPA) proposed ion channel panel. *J Pharmacol Toxicol Methods* 81:251e262
- Johannesen L, Vicente J, Mason JW, Sanabria C, Waite-Labott K, Hong M, Guo P, Lin J, Sørensen JS, Galeotti L, Florian J, Ugander M, Stockbridge N, Strauss DG (2014) Differentiating drug-induced multichannel block on the electrocardiogram: randomized study of dofetilide, quinidine, ranolazine, and verapamil. *Clin Pharmacol Therapeutics* 95(5):549–558
- Sahli Costabal F, Yao J, Sher A, Kuhl E (2019) Predicting critical drug concentrations and torsadogenic risk using a multiscale exposure-response simulator. *Prog Biophys Mol Biol* 144:61–76
- Redfern WS, Carlsson L, Davis AS, Lynch WG, MacKenzie II, Palethorpe S, Siegl PKS, Strang I, Sullivan AT (2003) Relationships between preclinical cardiac electrophysiology clinical QT interval prolongation and torsade de pointes for a broad range of drugs: evidence for a provisional safety margin in drug development. *Cardiovasc Res* 58(1):32–45
- Abaqus Analysis User's Guide (2020) Dassault Systèmes Simulia Corp
- Simo JC, Miehe CH (1992) Associative coupled thermoplasticity at finite strains: formulation, numerical analysis and implementation. *Comput Methods Appl Mech Eng* 98(1):41–104
- Holzappel GA, Ogden RW (2009) Constitutive modelling of passive myocardium: a structurally based framework for material characterization. *Philos Transact A Math Phys Eng Sci* 367(1902):3445–75
- Göktepe S, Abilez OJ, Kuhl E (2010) A generic approach towards finite growth with examples of athletes heart, cardiac dilation, and cardiac wall thickening. *J Mech Phys Solids* 58(10):1661–1680
- Gültekin O, Sommer G, Holzappel GA (2016) An orthotropic viscoelastic model for the passive myocardium: continuum basis and numerical treatment. *Comput Methods Biomech Biomed Eng* 19(15):1647–1664
- Walker JC, Ratcliffe MB, Zhang P, Wallace AW, Fata B, Hsu EW, Saloner D, Guccione JM (2005) MRI-based finite-element analysis of left ventricular aneurysm. *Am J Physiol Heart Circ Physiol* 289(2):H692–H700
- Sack KL, Aliotta E, Ennis DB, Choy JS, Kassab GS, Guccione JM, Franz T (2018) Construction and validation of subject-specific biventricular finite-element models of healthy and failing swine hearts from high-resolution DT-MRI. *Front Physiol* 9:539
- Peirlinck M, Sack KL, De Backer P, Morais P, Segers P, Franz T, De Beule M (2019) Kinematic boundary conditions substantially impact in silico ventricular function. *Int J Numer Methods Biomed Eng* 35(1):e3151
- Baillargeon B, Rebelo N, Fox DD, Taylor RL, Kuhl E (2014) The living heart project: a robust and integrative simulator for human heart function. *Eur J Mech A Solids* 48:38–47
- Peirlinck M, Sahli Costabal F, Yao J, Guccione JM, Tripathy S, Wang Y, Ozturk D, Segars P, Morrison TM, Levine S, Kuhl E (2021) Precision medicine in human heart modeling: perspectives, challenges, and opportunities. *Biomech Model Mechanobiol* 20(3):803–831
- Zygote Media Group Inc (2014) Zygote Solid 3D Heart Generations I & II Development Report. Technical Development of 3D Anatomical Systems
- Lombaert H, Peyrat JM, Croisille P, Rapacchi S, Fanton L, Cheriet F, Clarysse P, Magnin I, Delingette H, Ayache N (2012) Human

- atlas of the cardiac fiber architecture: study on a healthy population. *IEEE Trans Med Imag* 31(7):1436–1447
33. Bayer JD, Roney CH, Pashaei A, Jais P, Vigmond EJ (2016) Novel radiofrequency ablation strategies for terminating atrial fibrillation in the left atrium: a simulation study. *Front Physiol* 7:1–14
  34. Sahli Costabal F, Concha FA, Hurtado DE, Kuhl E (2017) The importance of mechano-electrical feedback and inertia in cardiac electromechanics. *Comput Methods Appl Mech Eng* 320:352–368
  35. Pezzuto S, Hake J, Sundness J (2016) Space-discretization error analysis and stabilization schemes for conduction velocity in cardiac electrophysiology. *Int J Numer Methods Biomed Eng* 32(10):e02762
  36. Augustin CM, Neic A, Liebmman M, Prassl AJ, Niederer SA, Haase G, Plank G (2016) Anatomically accurate high resolution modeling of human whole heart electromechanics: a strongly scalable algebraic multigrid solver method for nonlinear deformation. *J Comput Phys* 305:622–646
  37. Niederer S, Kerfoot E, Benson AP, Bernabeu MO, Bernus O, Bradley C, Cherry EM, Clayton R, Fenton FH, Garny A, Heidenreich E, Land S, Maleckar M, Pathmanathan P, Plank G, Rodríguez JF, Roy I, Sachse FB, Seemann G, Skavhaug O, Smith NP (2011) Verification of cardiac tissue electrophysiology simulators using an N-version benchmark. *Philos Trans A Math Phys Eng Sci* 369(1954):4331–51
  38. Perotti LE, Krishnamoorthi S, Borgstrom NP, Ennis DB, Klug WS (2015) Regional segmentation of ventricular models to achieve repolarization dispersion in cardiac electrophysiology modeling. *Int J Numer Methods Biomed Eng* 28:e02718
  39. Okada J, Washio T, Maehara A, Momomura S, Sugiura S, Hisada T (2011) Transmural and apicobasal gradients in repolarization contribute to T-wave genesis in human surface ECG. *Am J Physiol Heart Circul Physiol* 301(1):H200–H208
  40. Sahli Costabal F, Hurtado DE, Kuhl E (2016) Generating Purkinje networks in the human heart. *J Biomech* 49:2455–2465
  41. Ponnaluri AVS, Perotti LE, Ennis DB, Klug WS (2016) A viscoactive constitutive modeling framework with variational updates for the myocardium. *Comput Methods Appl Mech Eng* 314:85–101
  42. Bordas R, Gillow K, Lou Q, Efimov IR, Gavaghan D, Kohl P, Grau V, Rodríguez B (2011) Rabbit-specific ventricular model of cardiac electrophysiological function including specialized conduction system. *Prog Biophys Mol Biol* 107(1):90–100
  43. Kotikanyadanam M, Göktepe S, Kuhl E (2010) Computational modeling of electrocardiograms: a finite element approach toward cardiac excitation. *Int J Numer Methods Biomed Eng* 26(5):524–533
  44. Hii JTY, Wyse G, Gillis AM, Duff HJ, Solylo MA, Mitchell LB (1992) Precordial QT interval dispersion as a marker of Torsade de Pointes. *Circulation* 86:1376–1382
  45. Sadrieh A, Domanski L, Pitt-Francis J, Mann S, Hodgkinson EC, Ng CA, Perry MD, Taylor JA, Gavaghan D, Subbiah RN, Vandenberg J, Hill AP (2014) Multiscale cardiac modelling reveals the origins of notched T waves in long QT syndrome type 2. *Nat Commun* 5:5069
  46. Klabunde R (2011) Cardiovascular physiology concepts. Lippincott Williams & Wilkins, Philadelphia
  47. Gee MW, Förster C, Wall WA (2010) A computational strategy for prestressing patient-specific biomechanical problems under finite deformation. *Int J Numer Methods Biomed Eng* 26(1):52–72
  48. Peirlinck M, De Beule M, Segers P, Rebelo N (2018) A modular inverse elastostatics approach to resolve the pressure-induced stress state for in vivo imaging based cardiovascular modeling. *J Mech Behav Biomed Mater* 85:124–133
  49. Dessertenne F (1966) La tachycardie ventriculaire a deux foyers opposes variables. *Arch Mal Coeur Vaiss* 2(59):263–272
  50. Johnston J, Pal S, Nagele P (2013) Perioperative torsade de pointes: a systematic review of published case reports. *Anesth Analg* 117(3):559
  51. Vandael E, Vandenberg B, Vandenberghe J, Pincé H, Willems R, Foulon V (2017) Incidence of torsade de pointes in a tertiary hospital population. *Int J Cardiol* 243:511–515
  52. Hurtado DE, Rojas G (2018) Non-conforming finite-element formulation for cardiac electrophysiology: an effective approach to reduce the computation time of heart simulations without compromising accuracy. *Comput Mech* 61(4):485–497
  53. Margara F, Wang ZJ, Levrero-Florencio F, Santiago A, Vázquez M, Bueno-Orovio A, Rodríguez B (2021) In-silico human electromechanical ventricular modelling and simulation for drug-induced pro-arrhythmia and inotropic risk assessment. *Progress in Biophys Mol Biol* 159:58–74. <https://doi.org/10.1016/j.pbiomolbio.2020.06.007>
  54. Kılıçgedik A, Kahveci G, Gurbuz AS, Karabay CY, Guler A, Efe SC, Aung SM, Arslantas U, Demir S, Izgi IA (2017) Papillary muscle free strain in patients with severe degenerative and functional mitral regurgitation. *Arq Bras Cardiol* 108(4):339–346
  55. Perotti LE, Verzhbinsky IA, Moulin K, Cork TE, Loecher M, Balzani D, Ennis DB (2020) Estimating cardiomyofiber strain in vivo by solving a computational model. *Med Image Anal* 68:101932
  56. Wang TKM, Kwon DH, Griffin BP, Flamm SD, Popović ZB (2020) Defining the reference range for left ventricular strain in healthy patients by cardiac MRI measurement techniques: systematic review and meta-Analysis. *Am J Roentgenol* 217(3):569–583
  57. Wang TKM, Grimm RA, Rodríguez LL, Collier P, Griffin BP, Popović ZB (2021) Defining the reference range for right ventricular systolic strain by echocardiography in healthy subjects: a meta-analysis. *PLoS ONE* 16(8):e0256547
  58. Colatsky T, Fermini B, Gintant G, Pierson JB, Sager P, Sekino Y, Strauss DG, Stockbridge N (2016) The comprehensive in vitro proarrhythmia assay (CiPA) initiative-update on progress. *J Pharmacol Toxicol Methods* 81:15–20
  59. Fermini B, Hancox JC, Abi-Gerges N, Bridgland-Taylor M, Chaudhary KW, Colatsky T, Correll K, Crumb W, Damiano B, Erdemli G, Gintant G (2016) A new perspective in the field of cardiac safety testing through the comprehensive in vitro proarrhythmia assay paradigm. *J Biomol Screen* 21(1):1–11
  60. Dutta S, Chang KC, Beattie KA, Sheng J, Tran PN, Wu WW, Wu M, Strauss DG, Colatsky T, Li Z (2017) Optimization of an in silico cardiac cell model for Proarrhythmia risk assessment. *Front Physiol* 8:616
  61. Tomek J, Bueno-Orovio A, Passini E, Zhou X, Mincholé A, Britton O, Bartolucci C, Severi S, Shrier A, Virag L, Varro A (2019) Development, calibration, and validation of a novel human ventricular myocyte model in health, disease, and drug block. *Elife* 8:e48890
  62. Moss R, Wülfers EM, Schuler S, Loewe A, Seemann G (2022) A fully-coupled electro-mechanical whole-heart computational model: influence of cardiac contraction on the ECG. *Front Physiol* 12:778872
  63. Land S, Park-Holohan SJ, Smith NP, Dos Remedios CG, Kentish JC, Niederer SA (2017) A model of cardiac contraction based on novel measurements of tension development in human cardiomyocytes. *J Mol Cell Cardiol* 106:68–83
  64. Salvador M, Fedele M, Africa PC, Sung E, Dede L, Prakosa A, Crispin J, Trayanova N, Quarteroni A (2021) Electromechanical modeling of human ventricles with ischemic cardiomyopathy: numerical simulations in sinus rhythm and under arrhythmia. *Comput Biol Med* 136:104674
  65. Levrero-Florencio F, Margara F, Zacur E, Bueno-Orovio A, Wang ZJ, Santiago A, Aguado-Sierra J, Houzeaux G, Grau V, Kay D, Vázquez M (2020) Sensitivity analysis of a strongly-coupled human-based electromechanical cardiac model: effect of mechan-

- ical parameters on physiologically relevant biomarkers. *Comput Methods Appl Mech Eng* 361:112762
66. Fresca S, Manzoni A, Dedè L, Quarteroni A (2020) Deep learning-based reduced order models in cardiac electrophysiology. [arXiv:2006.03040](https://arxiv.org/abs/2006.03040)
67. Sahli Costabal F, Yang Y, Perdikaris P, Hurtado DE, Kuhl E (2020) Physics-informed neural networks for cardiac activation mapping. *Front Phys* 8:42
68. Regazzoni F, Salvador M, Dede L, Quarteroni A (2021) A machine learning method for real-time numerical simulations of cardiac electromechanics. [arXiv:2110.13212](https://arxiv.org/abs/2110.13212)
69. Peirlinck M, Sahli Costabal F, Sack KL, Choy JS, Kassab GS, Guccione JM, De Beule M, Segers P, Kuhl E (2019) Using machine learning to characterize heart failure across the scales. *Biomech Model Mechanobiol* 18:1987–2001

**Publisher's Note** Springer Nature remains neutral with regard to jurisdictional claims in published maps and institutional affiliations.